epic-AN-AC-2025-001

Precision Extraction of Momentum Transfer in Diffractive Coherent Exclusive Vector Meson Production

Principal Author List:
Maci Kesler (Kent State University, mkesler1@kent.edu)
Ashik Ikbal Sheikh (Kent State University, ashikhep@gmail.com)
Rongrong Ma (Brookhaven National Lab, marr@bnl.gov)
Zhoudunming Tu (Brookhaven National Lab, zhoudunming@bnl.gov)
Thomas Ullrich (Brookhaven National Lab, thomas.ullrich@bnl.gov)
Zhangbu Xu (Kent State University, Brookhaven National Lab, zxu22@kent.edu)

(December 15, 2025)

Abstract

Exclusive diffractive vector meson production is a critical component of the e+A program at the EIC. The exclusivity of the event makes it an experimentally clean and ideal measurement to study the onset of saturation and other QCD phenomena. Diffractive processes, $e{+}A \rightarrow e'{+}A'{+}VM$ *where* $VM = J/\psi, \phi$*, etc., allow the measurement of momentum transfer (*$|t|$*). A Fourier-Bessel transformation of* $|t|$ *enables us to extract the spatial distribution of the gluons inside the nucleus. This analysis focuses on improving the precision of the extraction of* $|t|$*.*

Contents

List of Figures

List of Tables

1 Introduction

The goal of this analysis is to advance the measurement of the nuclear momentum transfer distribution ($|t|$) through coherent exclusive vector meson (VM) production. Coherent exclusive VM production is considered a golden channel for imaging the gluon structure in nuclei and testing QCD properties, such as saturation [2]. Figure 1 shows the process of exclusive VM production. The incoming electron (e) emits a virtual photon (γ^*) which then fluctuates into a quark-antiquark pair (q and $\bar{q}$ respectively) which interacts with the target (A) via a Pomeron and then recombines to form the final state VM ($\phi \rightarrow K^+K^-$ in this analysis). The momentum transfer distribution forms a diffractive pattern that encodes information about the spatial distribution of gluons in the hadron wave function [3]. Since $|t|$ is conjugate to the impact parameter, a Fourier-Bessel (Hankel) transformation of the distribution enables us to obtain the spatial profile of the gluon density.

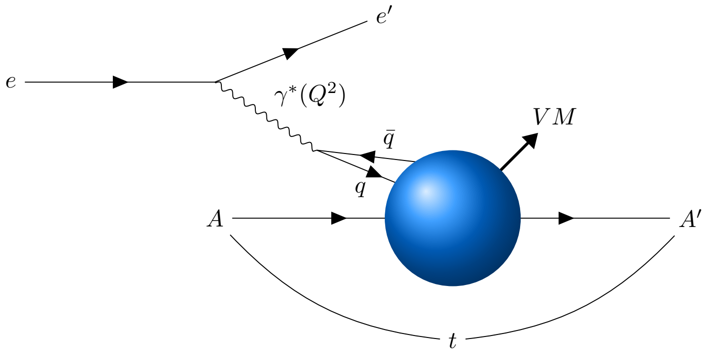

Figure 1: Diagram of coherent exclusive VM production.

We define the Mandelstam variable $|t|$ as

$$|t| = -(P_{\mathrm{A}'} - P_{\mathrm{A}})^2, \tag{1}$$

where $p_{\mathrm{A}'}$ and p_{A} denote the four-momenta of the outgoing and incoming nucleus. However, the $|t|$ distribution is a challenging measurement, as it depends on the outgoing nucleus' momentum, which, for heavy nuclei, we cannot access precisely. Consequently, we have to use different methods to reconstruct this measurement. There are two main complications with this: limited precision and a large background from incoherent production where the nucleus breaks up. This analysis utilizes a projective technique, as demonstrated in [4], to reconstruct the $|t|$ distribution.

After constructing the momentum transfer profile, we can take a Fourier-Bessel transformation to extract the spatial distribution of the gluons [5]. As shown in [6], a 2-dimensional transformation of the transverse $|t|$ distribution gives the transverse distribution of the spatial profile. The transformation used is given by

$$F(b) \propto \frac{1}{2\pi} \int_0^\infty d\Delta_\mathrm{T} \Delta_\mathrm{T} J_0(b\Delta_\mathrm{T}) \sqrt{\frac{d\sigma}{d|t|}}, \tag{2}$$

where J_0 is a Bessel function of the first kind and Δ_T is the transverse momentum. This analysis confirms the improvement of the measurement of the $|t|$ distribution which facilitates gluon imaging.

2 Simulation Overview

The Sartre event generator was used to simulate coherent exclusive ρ production for the purpose of a background study as well as coherent exclusive ϕ production. All energy configurations in this analysis are for 10x100 GeV beams. The cross sections for the simulated datasets are listed in Table 1.

For the ϕ files, the detector geometry, `CraterLake 25.10.2`, can be found on the ePIC Campaign Simulation webpage [7]. The specific files used are under `epic_craterlake/EXCLUSIVE/DIFFRACTIVE_PHI_ABCONV/sartre1.39-1.0/eAu/coherent/bsat/10x100`. These files are also accessible via `eic-shell` by the following commands:

- `xrdfsroot://dtn-eic.jlab.org`
- `ls /volatile/eic/EPIC/RECO/25.10.2/epic_craterlake/EXCLUSIVE/DIFFRACTIVE_PHI_ABCONV/sartre1.39-1.0/eAu/coherent/bsat/10x100`

A total of 2352 files were used under the base name of `sartre1.39-1.0_coherent_phi_eAu_bsat_10x100_ab.*.eicrecon.edm4eic.root`, where $*$ indicates a wildcard.

Similarly, for the ρ files, the detector geometry is `CraterLake 25.10.3` and the specific files are under `epic_craterlake/EXCLUSIVE/DIFFRACTIVE_RHO_ABCONV/sartre1.39-1.1/eAu/coherent/bsat/10x100/q2_1to20`. 2255 files were used in this analysis under the base name of `sartre1.39-1.1_coherent_rho_eAu_bsat_10x100_q2_1to20_hiAcc.*.eicrecon.edm4eic.root`.

The BeAGLE event generator was used to simulate inclusive DIS events for the purpose of a background study as well as for incoherent production of diffractive ϕ. These files are also accessible via `eic-shell` and retrieved in the same way as stated above.

For the DIS files, the detector geometry is from `CraterLake 25.10.2`. The specific files used are under `epic_craterlake_without_zdc/DIS/BeAGLE1.03.02-1.0/eAu/10x100/q2_1to10`, where 4998 files were used. The files have a base name of `BeAGLE1.03.02-1.0_DIS_eAu_10x100_q2_1to10_ab_run*.eicrecon.edm4eic.root`.

For the incoherent files, the detector geometry is from `CraterLake 25.10.3`, with the file names being under `epic_craterlake/EXCLUSIVE/DIFFRACTIVE_PHI_ABCONV/BeAGLE1.`

`03.02-1.1/eAu/10x100/q2_1to10000`, where 2599 files were used and have a base name of `BeAGLE1.03.02-1.1_phi_eAu_10x100_q2_1to10000_hiAcc_run*.eicrecon.edm4eic.root`.

Note that campaigns 10.25.2 and 10.25.3 were both used in this analysis. There was a memory issue in 10.25.2 but the results of the changes to 10.25.3 do not affect my analysis. Further information about this can be found on the Github [8].

Table 1: Cross sections for simulated datasets.

Dataset	**Cross section (σ) [nb]**
Sartre coherent diffractive ϕ	$\sigma_\phi = 459.05$
BeAGLE incoherent diffractive ϕ	$\sigma'_\phi = 261.95$
Sartre coherent diffractive ρ	$\sigma_\rho = 5418.68$
BeAGLE DIS background	$\sigma_{DIS} = 50184.8$

2.1 Event Generator Details

The version of Sartre used is 1.39-1.0 for coherent diffractive ϕ production and 1.39-1.1 for coherent diffractive ρ. More details on the Sartre event generator can be found in [9, 10] while detailed information regarding the simulated data set can be found on GitHub [11]. The versions of BeAGLE used for incoherent ϕ production and DIS inclusive background are BeAGLE1.03.02-1.1 and BeAGLE1.03.02-1.0 respectively. They can both be found on GitHub [12]. For more information on the BeAGLE event generator, see [13].

3 Event Selection

3.1 The Code Logic

The code processes the events from the Sartre and BeAGLE files and reconstructs the kinematics for the beam particles, scattered electrons (e'), and produced VMs. This analysis uses different methods to reconstruct the $|t|$ distribution by invoking cuts and momentum projection along the direction normal to the electron scattering plane ($\hat{n}$), as shown in Fig. 2, to resolve the diffractive pattern and the resulting gluon distribution through a Fourier-Bessel transformation.

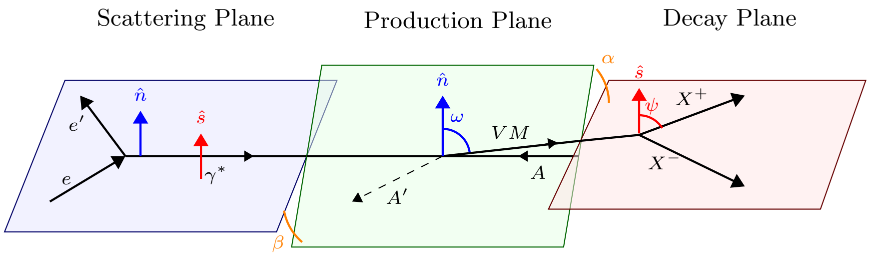

Figure 2: Diagram of exclusive VM production. The blue arrow indicates the normal direction, $\hat{n}$, from the electron scatting plane. The red arrow show the spin direction of the emitted virtual photon. The VM production and decay planes are also shown. β is the angle between the scattering plane and the production plane, α is the angle between the production plane and the decay plane, and ω is the angle measured from the $\hat{n}$ direction ($\omega = \pi/2 - \beta$).

3.1.1 Breakdown: the analysis

Each iteration of the event reading loop processes one event from the input tree. The events are processed in the following way:

- Build Monte Carlo (MC) particles:
  - Loop over MC particles (which represent the truth) to identify the electron, beam particle, e', and the VM decay daughters produced (in this analysis $\phi \rightarrow K^+K^-$).
    - If studying $\rho \rightarrow \pi^+\pi^-$ background contamination, the VM daughters will be assigned accordingly
- Build reconstructed particles:
  - Technique for e' (Note that this method implements the electron finding method [14], but at the time of writing this, the energy isolation cut has not yet been implemented):
    - Find the highest energy cluster in the electron end cap by looping over the electromagnetic calorimeter (EMCal) clusters. This is then defined as the maximum energy and is used to define the positions x and y.
    - Repeat this process, but instead look for the highest hit energy (above a threshold energy of 10 MeV) in the EMCal by looping over individual calorimeter cells and store that energy and position.
    - Build a 3x3 cluster around this position, mimicking calorimeter showers.
    - By summing nearby hit energies (within 70 mm of the maximum hit energy), we form a shower. This gives a better estimate of the total energy and position to reconstruct the particle energy and impact point.
    - Take the weighted average of this cluster position to define the final cluster position.

    - ∗ Add a 4.4% energy calibration to correct the EMCal energy response and define this as the final cluster energy.
    - ∗ Loop over the EMCal track to match the clusters to the track in x and y. This ensures that the EMCal cluster is associated with a particle track.
    - ∗ Lastly, we ensure that the reconstructed electron ID matches the MC electron ID and we require that the charge is negative.
    - ∗ After we find e', we impose the following selection cuts (details about this can be found in Sec. 3.2:
      - · e' must have energy ($E > 0$)
      - · $15 < E - p_z < 25$
      - · $0.8 < E/p < 1.2$
    - ∗ We then reconstruct e' using the electron method (see [14]).
  - – Loop over the tracks to build the hadronic final state (HFS) from all tracks, excluding e'.
    - ∗ This identifies the VM daughters produced, in this case, the kaons.
    - ∗ The HFS should be $\phi \to K^+K^-$ and e' since the event is coherent and exclusive.
  - – We then check that HFS== 2 and that those 2 particles are K^+ and K^-, if not then we veto it. Furthermore, we impose a mass selection to ensure that we are reconstructing the ϕ meson.
  - – Figures 3–6 show the energy and θ distributions from the resulting scattered electron.
  - – We enforce cuts on the reconstructed Q^2 and y which will be gone over in more detail in Sec. 3.2.

- Lastly, we check if there are hits in the off-momentum detectors (OMD), Roman Pots (RP), or zero-degree calorimeters (ZDC) to remove incoherent events. We do this by forming arrays from the OMDs, RPs, and ZDC. These are used for incoherent or background event vetoes. Note that we do not have branches for the B0 detector at the time of writing this so it is omitted in this analysis.

- Finally, we reconstruct $|t|$ using the techniques described in this note.

3.1.2 Breakdown: the transformation

The differential cross section is imported from the ROOT file generated after running the analysis described in Section 3.4.

- We first sample the differential cross section with Guassian smearing to propagate errors and statistical uncertainties by looping over 1000 trials.

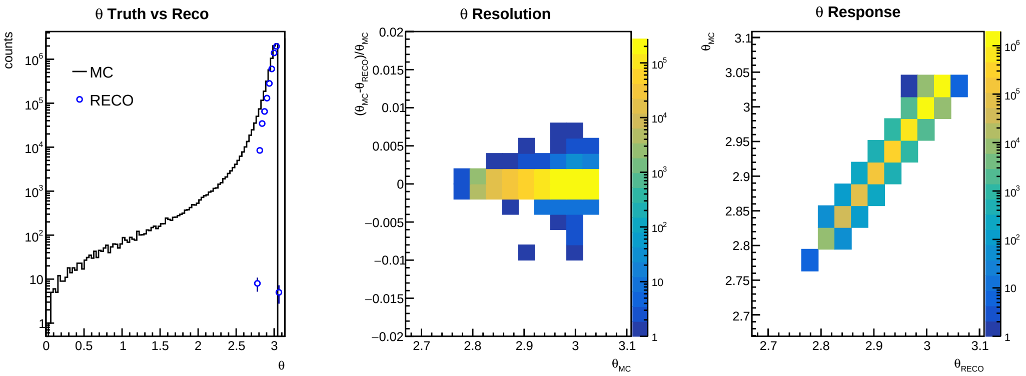

Figure 3: The leftmost plot shows the reconstruction of θ_e in comparison with the truth. The middle plot shows the resolution and the rightmost plot shows the response.

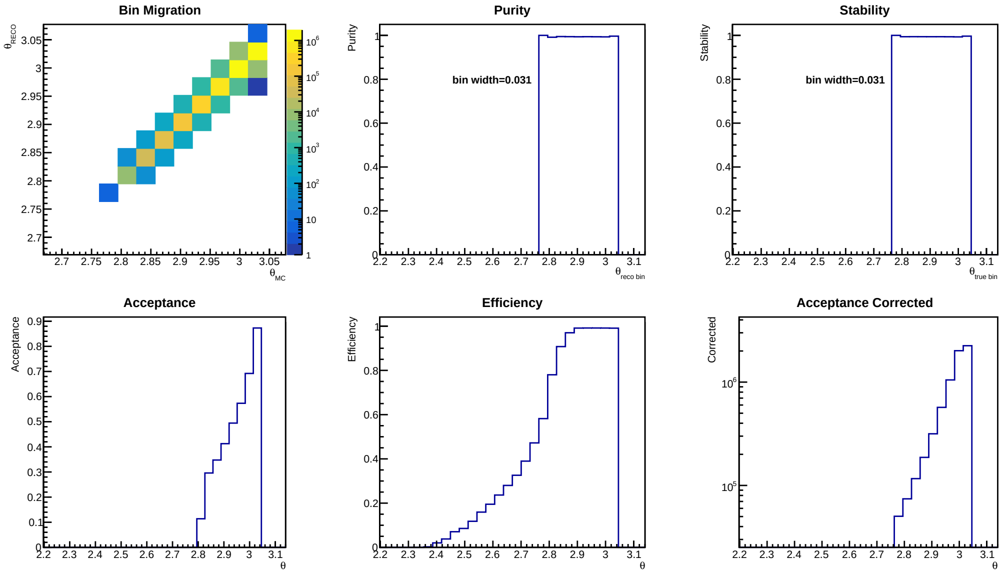

Figure 4: QA plots for θ_e.

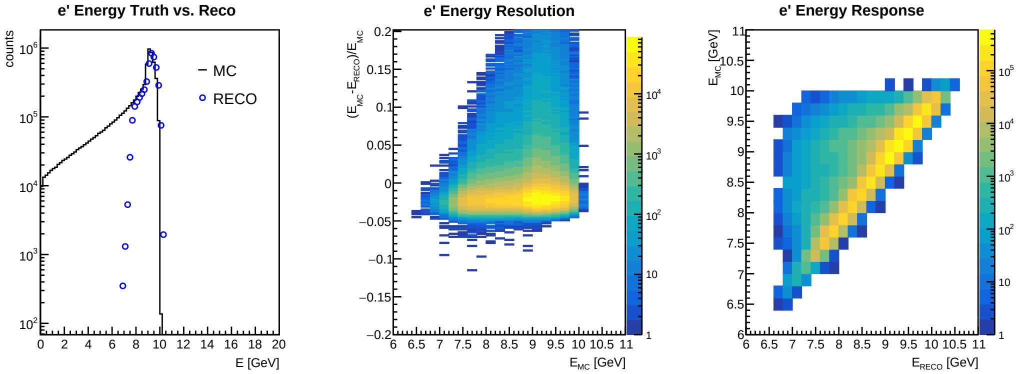

Figure 5: The leftmost plot shows the reconstruction of the energy of e' in comparison with the truth. The middle plot shows the resolution and the rightmost plot shows the response.

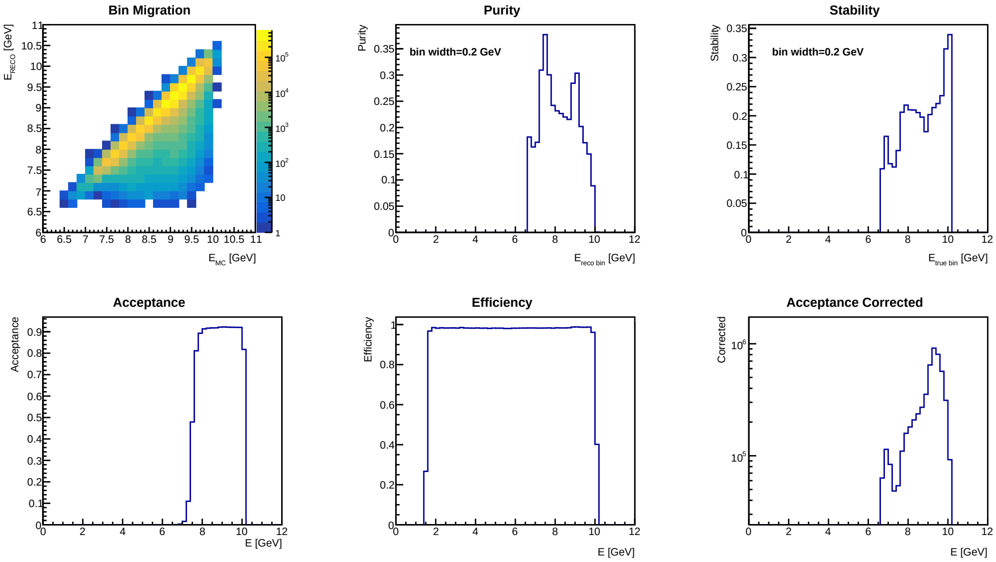

Figure 6: QA plots for the energy of e'.

- For each trial:
  - Loop over all bins and convert the differential cross section to amplitude (*i.e.* $d\sigma/d|t| \rightarrow \sqrt{d\sigma/d|t|}$).
  - Apply sign flips at each diffractive minima to maintain the oscillatory structure of the $|t|$ distribution as stated in [5,15].
  - Accumulate the weighted Fourier-Bessel transform contribution for each impact parameter bin.
- The resulting distributions in b (position-space) are averaged over trials, with RMS providing the uncertainty.

3.2 Cuts

The following cuts have been made on the reconstruction level. The kinematic variables Q^2, y, and x have been reconstructed following the algorithm and cuts for the electron finder found here [14]. Table 2 summarizes all cuts on kinematic variables and this section will go through each one in more detail.

- Phase space: We have a cut on the virtuality of the photon which is defined as

$$Q^2_{\mathrm{MC}} = 2E_{e'_{\mathrm{MC}}} E_{e_{\mathrm{MC}}}[1 + \cos(\theta_{e'_{\mathrm{MC}}})], \tag{3}$$

where $E_{e'_{\mathrm{MC}}}$ and $E_{e_{\mathrm{MC}}}$ are the energy of the incoming and scattered electron respectively and $\theta_{e'_{\mathrm{MC}}}$ is the polar angle of the scattered electron. The subscripts MC and RECO

Table 2: Summary of cuts applied at MC and reconstruction level.

Variable	**Cut Value / Range**	**Level**	**Purpose**
Q^2	$1 < Q^2 < 10$ GeV^2	MC + RECO	Ensure hard photon, avoid poor resolution
y (inelasticity)	$0.01 < y < 0.85$	MC + RECO	Avoid trivial interactions and extreme energy loss
VM energy	$E_{\text{VM}} > 0$	MC + RECO	Require produced vector meson
VM mass	$\|m_{\text{VM}} - 1.02\| < 0.02$ GeV/c^2	RECO	Select ϕ meson
$E - p_z$ (for e')	$15 < E - p_z < 25$ GeV	RECO	Ensure exclusivity
E/p (for e')	$0.8 < E/p < 1.2$	RECO	Match EMCal energy to track momentum
$\|t\|$ projection angle	$\omega < \omega_{\max}$	MC + RECO	Minimize VM momentum in electron scattering plane

indicate whether we use the Monte Carlo distribution or the reconstructed one. We reconstruct the virtuality given by

$$Q^2_{\text{RECO}} = 2E_{e'_{\text{RECO}}} E_{e_{\text{MC}}}[1 + \cos(\theta_{e'_{\text{RECO}}})], \tag{4}$$

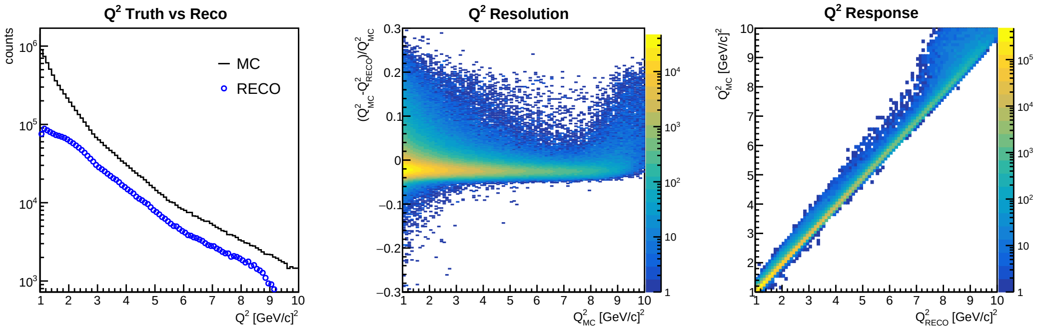

Figure 7: The leftmost plot shows the reconstruction of Q^2 in comparison with the truth. The middle plot shows the resolution and the rightmost plot shows the response.

An additional cut is placed on the fractional energy lost by the electron (inelasticity) expressed as

$$y_{\text{MC}} = 1 - \left(\frac{E_{e'_{\text{MC}}}}{E_{e_{\text{MC}}}}\right) \sin\left(\frac{\theta_{e'_{\text{MC}}}}{2}\right). \tag{5}$$

The inelasticity is reconstructed by the following

$$y_{\text{RECO}} = 1 - \left(\frac{E_{e'_{\text{RECO}}}}{E_{e_{\text{MC}}}}\right) \sin\left(\frac{\theta_{e'_{\text{RECO}}}}{2}\right). \tag{6}$$

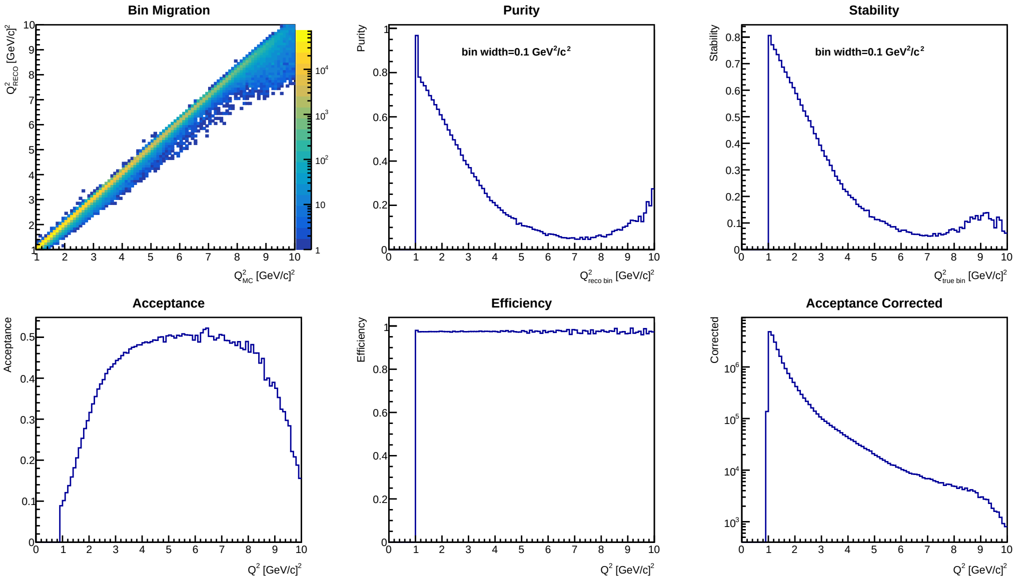

Figure 8: QA plots for the Q^2 variable.

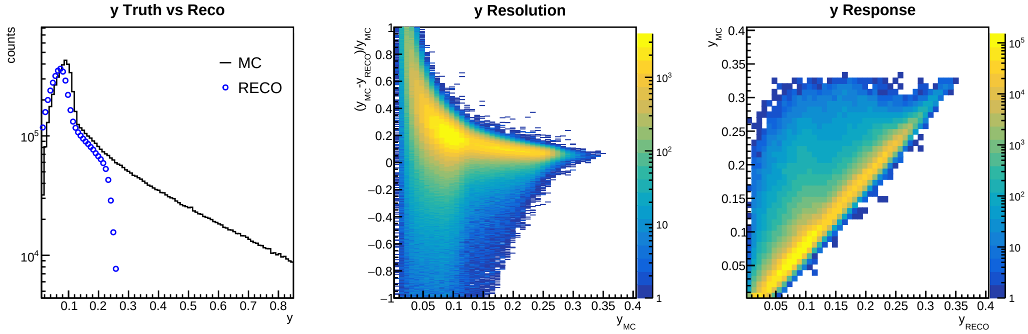

Figure 9: The leftmost plot shows the reconstruction of y in comparison with the truth. The middle plot shows the resolution and the rightmost plot shows the response.

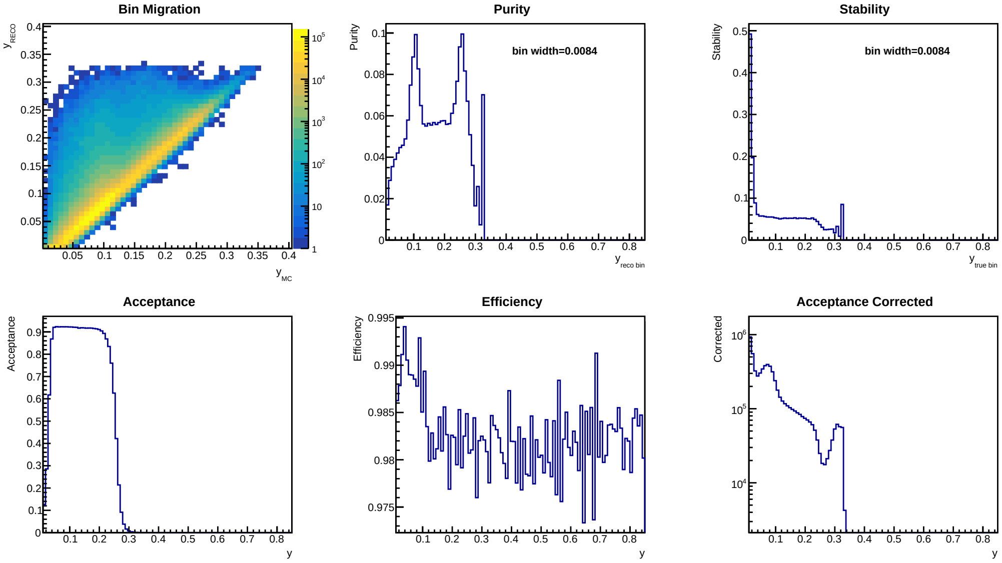

Figure 10: QA plots for y.

We define the Bjorken-x variable, fraction of the hadrons momentum carried by the parton that the electron scatters from, as

$$x_{\text{MC}} = \frac{Q^2_{\text{MC}}}{4E_{e_{\text{MC}}}E_{Au_{\text{MC}}}y_{\text{MC}}}, \tag{7}$$

where $E_{Au_{\text{MC}}}$ is the energy of the incoming gold beam. The reconstruction is defined as

$$x_{\text{RECO}} = \frac{Q^2_{\text{RECO}}}{4E_{e_{\text{MC}}}E_{Au_{\text{MC}}}y_{\text{RECO}}}. \tag{8}$$

By putting constraints on these kinematic variables, we are able to isolate a clean, reliable region. For the virtuality, we have $Q^2 > 1$ to ensure that the photon is hard enough to resolve the partons and $Q^2 < 10$ to aviod events with poor resolution. For

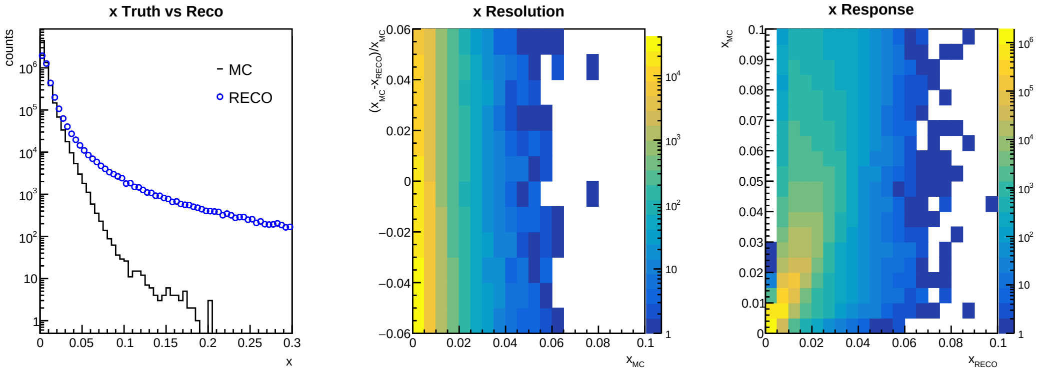

Figure 11: The leftmost plot shows the reconstruction of x in comparison with the truth. The middle plot shows the resolution and the rightmost plot shows the response.

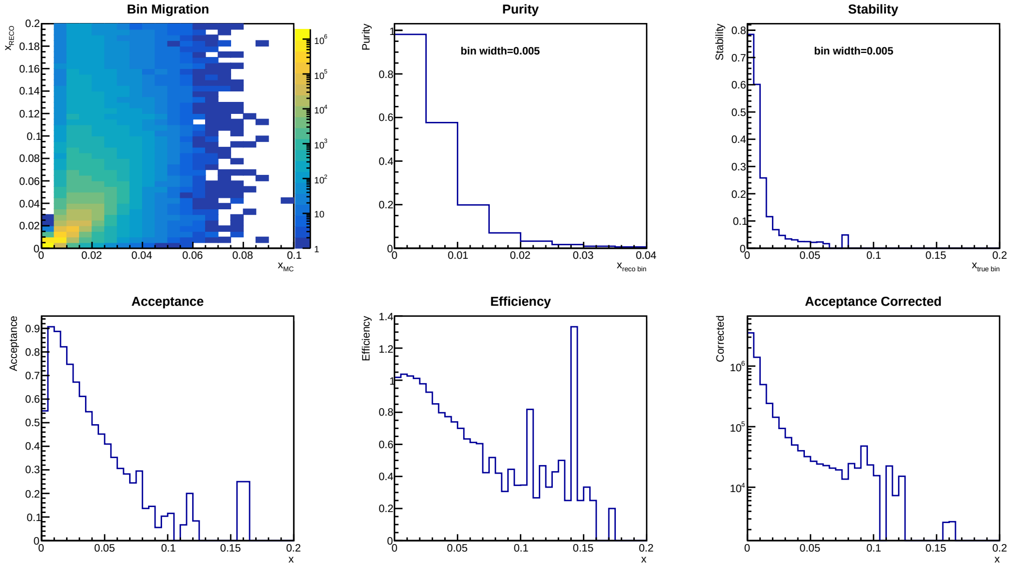

Figure 12: QA plots for x.

the inelasticity, we have $y > 0.01$ to avoid events where the electron barely interacts and $y < 0.85$ to avoid events where the electron loses almost all of it's energy. The resulting Q^2, y, and x distributions are shown in Figs. 7, 9, and 11. For reference and quality assurance (QA), Figs. 8, 10, and 12 show the results from this analysis.

We define the QA checks in the following way (note that unfolding will be done in future work as we plan to integrate deep learning models to perform this task):

- Bin migration: Events in true bin i reconstructed in bin j. Ideally this would be a diagonal to show that events are properly reconstructed.
- Purity: Ratio of correctly reconstructed events in MC bin and the total reconstructed events. High purity corresponds to less contamination from neighboring bins. We want values to be close to 1.

$$\text{Purity} = \frac{N_{j\to j}}{\Sigma_i N_{i\to j}} \tag{9}$$

- Stability: Ratio of events in a given MC bin that are reconstructed into the same bin. High stability corresponds to events staying in their bin.

$$\text{Stability} = \frac{N_{i\to i}}{\Sigma_j N_{i\to j}} \tag{10}$$

- Acceptance: Fraction of true events that are reconstructed anywhere and survive the selection cuts. This should be a smooth distribution whereas sharp fluctuations indicate a cut boundary or detector geometry edge. We want values to be close to 1.

$$\text{Acceptance} = \frac{\Sigma_j N_{i\to j}}{N_i^{\text{true}}} \tag{11}$$

  - Efficiency: Ratio of true events that are reconstructed and pass final selection criteria.

$$\text{Efficiency} = \frac{N^{\text{reco bin } i}}{N_i^{\text{true}}} \tag{12}$$

  - Corrected: Acceptance-corrected yield per true bin. This should be comparable to the MC truth distribution.

$$\text{Corrected} = \frac{N^{\text{reco bin } i}}{\text{Acceptance}} \tag{13}$$

- Vector Meson: We reject events where the VM has zero energy to confirm that we skip events without a produced VM. Furthermore, we want to look at regions where the VM is produced centrally to verify that we have a distinct diffractive event. This is done by placing a cut on the VM rapidity which defines how forward or backward a particle is moving in the beam direction. For this reason, we place a constraint on the VM rapidity to be $|y_\phi| < 3.5$. Lastly, we use the constraint $|m_{\text{VM}} - 1.02|$ GeV/c^2 < 0.02 GeV/c^2 to ensure that we are selecting ϕ since $m_\phi \approx 1.02$ GeV/c^2. VM reconstruction is discussed in more detail in Section 3.2.1 and is shown in Figs. 14 and 16 while the QA plots are presented in Figs. 15 and 17.

- Momentum Distribution: For the new method presented in this analysis (projection method), we want to find the region of phase space where the four-momentum of the VM is dominate in the direction normal ($\hat{n}$) to the electron scattering plane [4]. The reason for this is that $|t|$ component along the $\hat{n}$ direction is unaffected by the momentum resolution e'. Therefore, we apply a cut on the angle between $\hat{n}$ and the direction of the scattered electron ($\hat{x}$). This minimizes the VMs four-momenta in the direction of the electron scattering plane. We do this by defining the angle $\omega_{\max} = \tan^{-1}(\Delta_x/\Delta_y)$ where

$$\begin{aligned} |t|_\perp &= \Delta_\perp^2 = \Delta_x^2 + \Delta_y^2 \\ \Delta_x &= \Delta_\perp \sin\omega \\ \Delta_y &= \Delta_\perp \cos\omega, \end{aligned} \tag{14}$$

  choosing the optimal angle needed for analysis. Figure 13 shows the 2-dimensional $|t|$ distribution where a cut of $\omega_{\max}$ is shown.

The following cuts have been made only on the reconstruction level of the events from the detector information (in addition to the cuts mentioned above).

- Event selection: Here, we choose $15 < E - p_z < 25$ GeV of the scattered electron to ensure exclusivity. Additionally, we implement a selection of $0.9 < E/p < 1.2$ to confirm that the EMCal energy matches the track momentum and that we select true electrons. The results of these cuts are shown in Figures 20 and 18 while the QA plots are shown in Figs. 21 and 19.

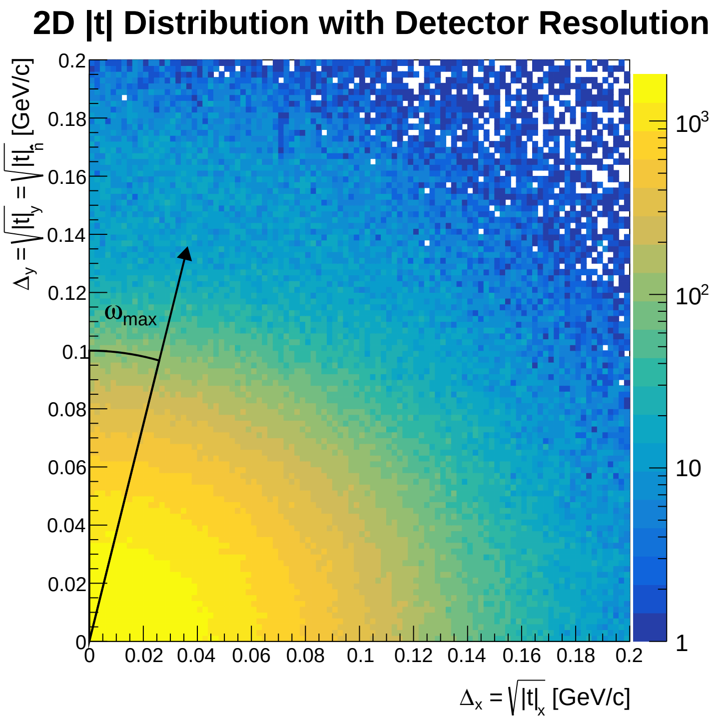

Figure 13: $|t| = \Delta^2$ distribution in 2-dimensions. The wedge cut is shown by the angle $\omega_{\max}$ to demonstrate the projection technique.

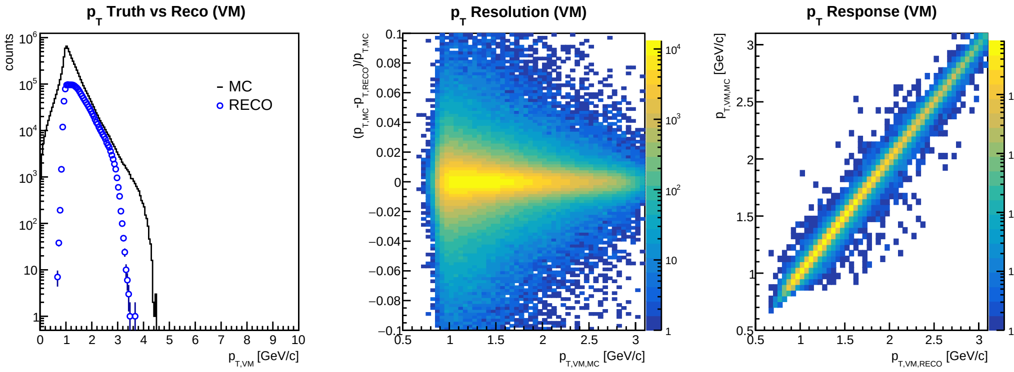

Figure 14: The leftmost plot shows the reconstruction of p_T for the VM in comparison with the truth. The middle plot shows the resolution and the rightmost plot shows the response.

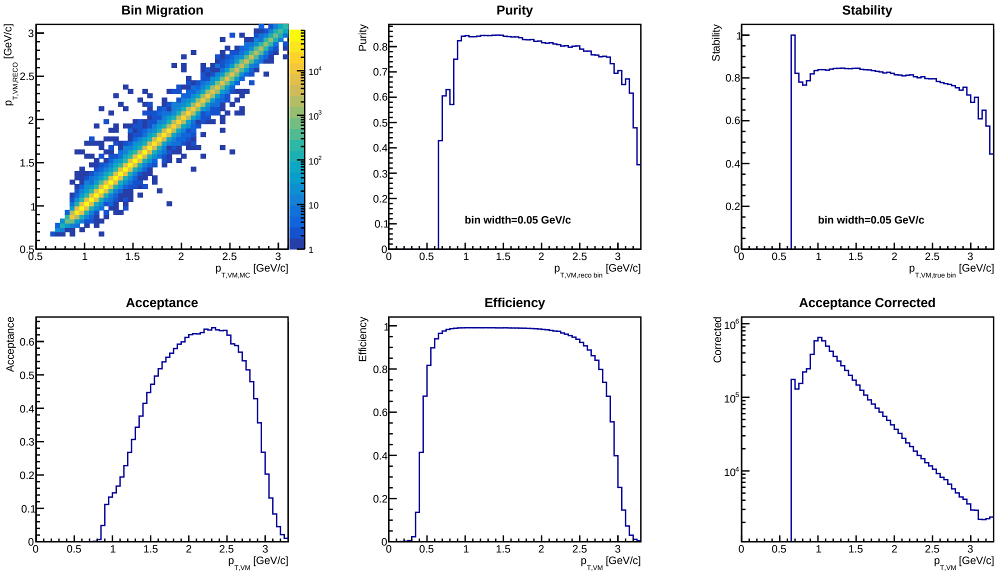

Figure 15: QA plots for the VMs p_T distribution.

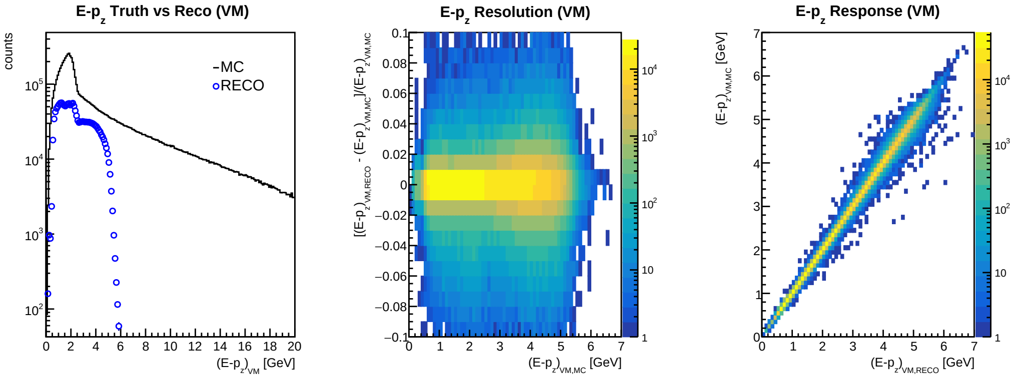

Figure 16: The leftmost plot shows the reconstruction of the $E - p_z$ distribution of the VM in comparison with the truth. The middle plot shows the resolution and the rightmost plot shows the response.

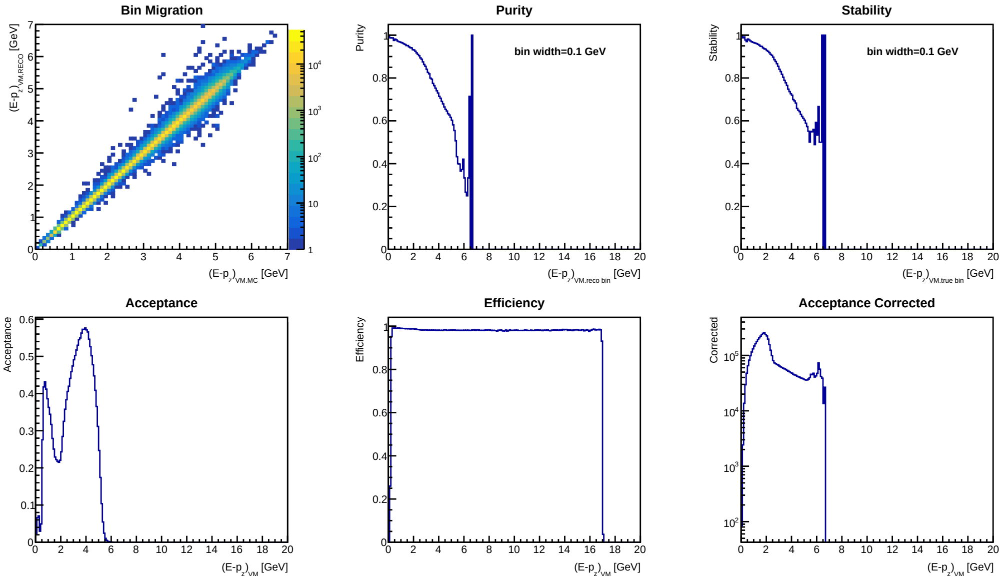

Figure 17: QA plots for the VMs $E - p_z$ distribution.

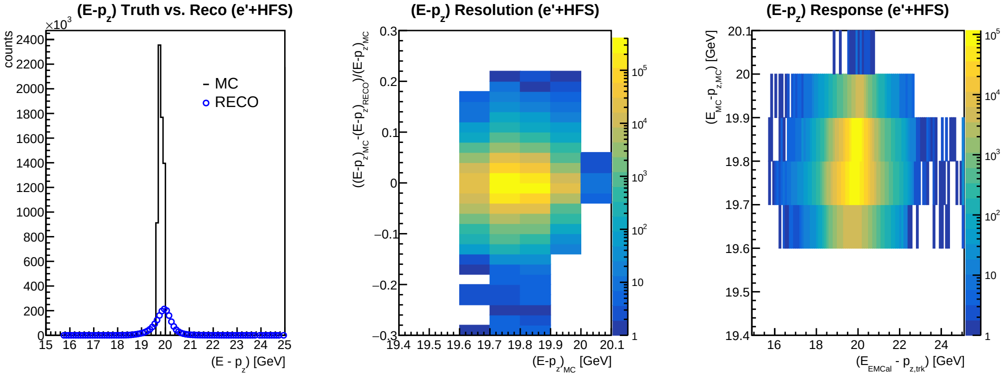

Figure 18: The leftmost plot shows the reconstruction of the $E - p_z$ distribution from e' in comparison with the truth. We expect this to peak around $2E_e = 20$ GeV. The middle plot shows the resolution and the rightmost plot shows the response.

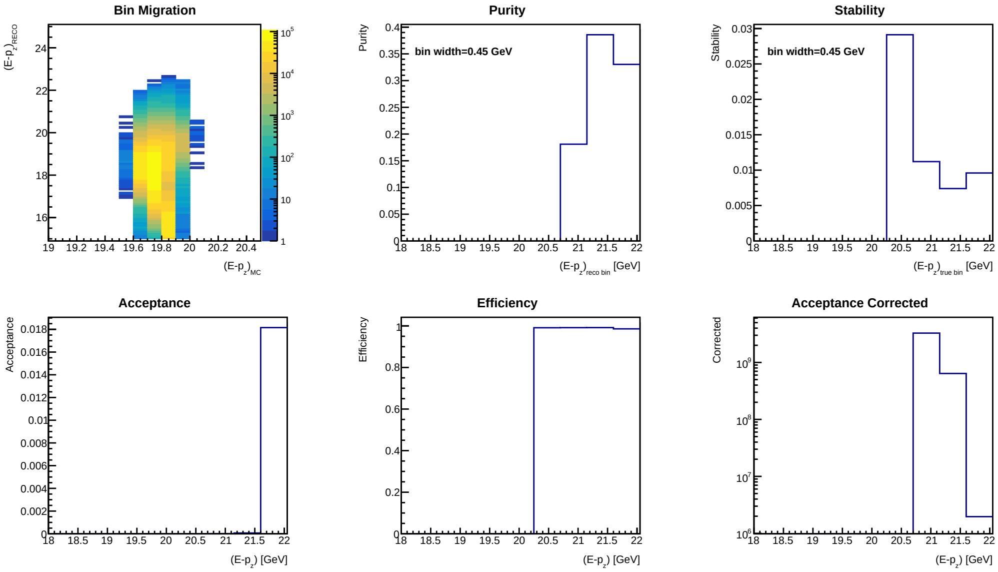
Bin Migration
Purity
Stability
Acceptance
Efficiency
Acceptance Corrected

Figure 19: QA plots for the $E - p_z$ distribution from e'.

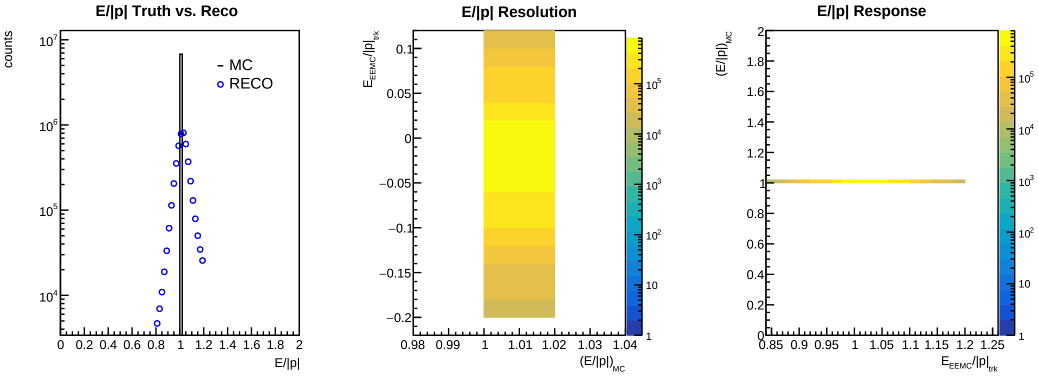
E/|p| Truth vs. Reco
E/|p| Resolution
E/|p| Response

Figure 20: The leftmost plot shows the reconstruction of $E/|p|$ for e' in comparison with the truth. We expect this to peak at one to demonstrate good matching of the EMcal with the track. The middle plot shows the resolution and the rightmost plot shows the response.

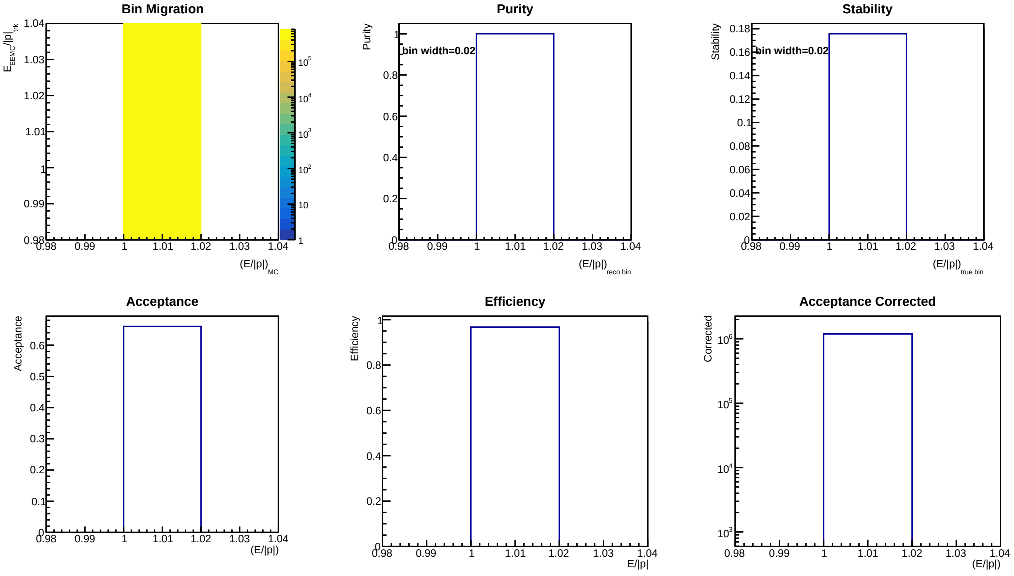
Bin Migration

Purity

Stability

Acceptance

Efficiency

Acceptance Corrected

Figure 21: QA plots for $E/|p|$ for e'.

3.2.1 Reconstruction Methods

The `MCParticles` branch is used to reconstruct the MC particle momentum, generator status, mass, and PDG arrays for each MC particle. To reconstruct the EMCal endcap clusters, we use the position and energy arrays from the `EcalEndcapNClusters` and `EcalEndcapNRecHits` branches. The `EcalEndcapNClusterAssociations` branch is used for the rec and sim ID arrays. We also reconstruct calorimeter tracks using the `_CalorimeterTrackProjections_points` branch for the position and momentum arrays. The `ReconstructedChargedParticles` branch is used to reconstruct the charged particles' momentum, rec and sim ID arrays, and charge. To reconstruct the ZDC events we use the branches HcalFarForwardZDC-Clusters and EcalFarForwardZDCClusters to get the position and energy arrays from the separate parts of the ZDC. The roman pots events are reconstructed using the branch `ForwardRomanPotRecHits` to get the position arrays. Lastly, we use the `ForwardOffMTrackerRecHits` branch to reconstruct the OMD position arrays. Some variables have special methods implemented for reconstruction, which will be explained in this section.

- VM: We loop over the track array to select the decay daughters. We then assign the positive and negative particles, in this case $K^{\pm}$.
- Scattered electron ($P_{e'_{\text{RECO}}}$): This variable is derived by using the EMCal cluster energy, E_{cal} (obtained from the EM hits array as described in section 3.1). E_{cal} is used to calculate the momentum ($p = \sqrt{E_{\text{cal}}^2 - m^2}$, where m is the mass of the electron). We then use that to calculate $p_T = p \sin\theta$ which allows us to define the scattered electron four-momentum in terms of m, η, ϕ, and p_T, where η, ϕ, and θ are resolved from the reconstructed track momentum array.

- Momentum transfer distribution ($|t|$): There are three different ways in this analysis that are implemented to reconstruct the $|t|$ distribution, method E, method L, and the projection method. Given a coherent exclusive diffractive VM event, we have the following conservation of four-momenta equation

  $$P_e + P_{\mathrm{A}} \rightarrow P_{e'} + P_{\mathrm{A'}} + P_{\mathrm{VM}}. \tag{15}$$

  The derivation of the different methods of $|t| = -(P_{A'} - P_A)^2$ reconstruction are based off of Eqn. 15 and given by the following:

  - Method E: Directly solves for $P_{\mathrm{A'}}$ to arrive at the final formula for $|t|$ and is used to generate MC events given by

    $$\begin{aligned} P_{\mathrm{A'}} &= P_e + P_{\mathrm{A}} - P_{e'} - P_{\mathrm{VM}} \\ |t|_{\mathrm{E}} &= -(P_{\mathrm{A'}} - P_{\mathrm{A}})^2 \\ &= -(P_e - P_{e'} - P_{\mathrm{VM}})^2. \end{aligned} \tag{16}$$

  - Method L: Uses a corrected outgoing ion momentum by using the mass as an additional constraint. We first change to light-cone variables defined as

    $$p_{\pm} = p_E \pm p_z \tag{17}$$

    $$p^2 = p_+ p_- - p_{\mathrm{T}}^2 = m^2 c^4. \tag{18}$$

    Solving for p_E and p_z gives

    $$p_z = p_+ - p_E \tag{19}$$

    $$p_E = p_- + p_z. \tag{20}$$

    Using the above equations you can solve for p_z and p_E in terms of p_+ and p_- resulting in

    $$p_z = \frac{p_+ - p_-}{2} \tag{21}$$

    $$p_E = \frac{p_- + p_+}{2}. \tag{22}$$

    Lastly, we use these new variables for $P_{\mathrm{A'}}^{\mathrm{corr}}$ to arrive at our new $|t|$ expressed as

    $$\begin{aligned} P_{\mathrm{A'}}^{\mathrm{corr}} &= (p_x, p_y, p_z, p_E) \\ &= \left(p_x, p_y, \frac{p_+ - p_-}{2}, \frac{p_- + p_+}{2}\right) \end{aligned} \tag{23}$$

    $$|t|_{\mathrm{L}} = -(P_{\mathrm{A'}}^{\mathrm{corr}} - P_{\mathrm{A}})^2. \tag{24}$$

  - Projection method: Incorporates a wedge cut as an additional requirement for method L. We define the projected $|t|$ as

    $$|t|_{\mathrm{proj}} = (|t|_x, |t|_{\hat{n}}, |t|_z, |t|_E), \tag{25}$$

    where

    $$|t|_{\hat{n}} = -[(P_e - P_{e'} - P_{\mathrm{VM}}) \cdot \hat{n}]^2 \tag{26}$$

    $$= (P_{\mathrm{VM}} \cdot \hat{n})^2. \tag{27}$$

- ∗ Beginning with the $|t|$ distribution given by method L, we decompose as $|t| = |t|_\perp + |t|_{//}$ where $|t|_\perp = |t|_x + |t|_y$ and $|t|_{//} = |t|_z + |t|_E$ are transverse and longitudinal components respectively.
- ∗ We further decompose the transverse components such that $\Delta_x = \sqrt{|t|_x}$ and $\Delta_y = \sqrt{|t|_y}$ (i.e. $\Delta_y = \Delta_{\hat{n}} = \sqrt{|t|_y} = \sqrt{|t|_{\hat{n}}}$ given the relation $|t|_\perp = \Delta_\perp^2 = \Delta_x^2 + \Delta_y^2$).
- ∗ We then parameterize p_x and p_y for which

$$\begin{aligned} \Delta_x &= \Delta_\perp \sin(\omega) \\ \Delta_y &= \Delta_\perp \cos(\omega). \end{aligned} \tag{28}$$

- ∗ Lastly, we cut a wedge of angle $\omega_{\max}$ from the $\Delta_y = \Delta_{\hat{n}}$ axis (see [4] for more details). The angle for the wedge cut is given by

$$\omega_{\max} = \tan^{-1}\left(\sqrt{\frac{|t|_x}{|t|_{\hat{n}}}}\right). \tag{29}$$

The result of the projection method including all of the cuts previously mentioned is shown in Fig. 22 using a cut of $\omega_{\max} = \pi/12$, the QA plots are shown in Fig. 3.2.1, and the resolution is shown in Fig. 25. Figure 23 shows the $|t|$ distribution with different $\omega_{\max}$ cuts. Note that all plots with a $|t|$ distribution that implements the projection method is normalized by $(\pi/2)/\omega_{\max}$ and all results for this analysis use an angle cut of $\omega_{\max} = \pi/12$.

3.3 Systematic Uncertainies

The dominant systematic uncertainty in this analysis arises from incoherent production, which cannot be fully removed by the applied selection cuts and detector vetoes. The incoherent detector vetoes are still under investigation. While ρ contamination is suppressed by PID requirements, DIS background and incoherent events remain and contribute to the measured distributions. Additional detector systematic effects will be implemented as the detector calibration and performance become better established. Figure 26 shows all background included in this analysis for the $|t|$ distribution without applying any additional vetoes, cuts, or PID. The following sections will review each systematic uncertainty individually.

3.3.1 DIS Background

We added DIS background as one source of systematic uncertainty. The result of adding it to our $|t|$ distribution is shown in Figure 28. We see that without any vetoes, the DIS background dominates the diffractive pattern. Upon adding the detector vetoes, most of the

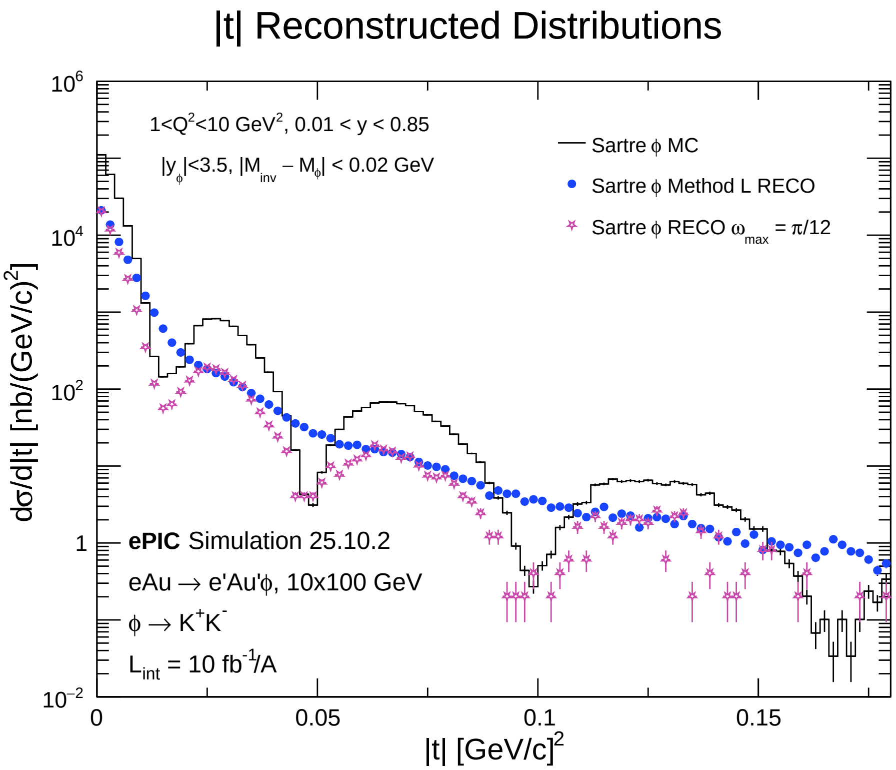

Figure 22: $|t|$ distribution where the black solid line represent the MC truth, the curve with blue dots corresponds to method L reconstruction, and the open pink stars correspond to $|t|$ reconstruction using the projection method with a wedge cut of $\omega_{\max} = \pi/12$.

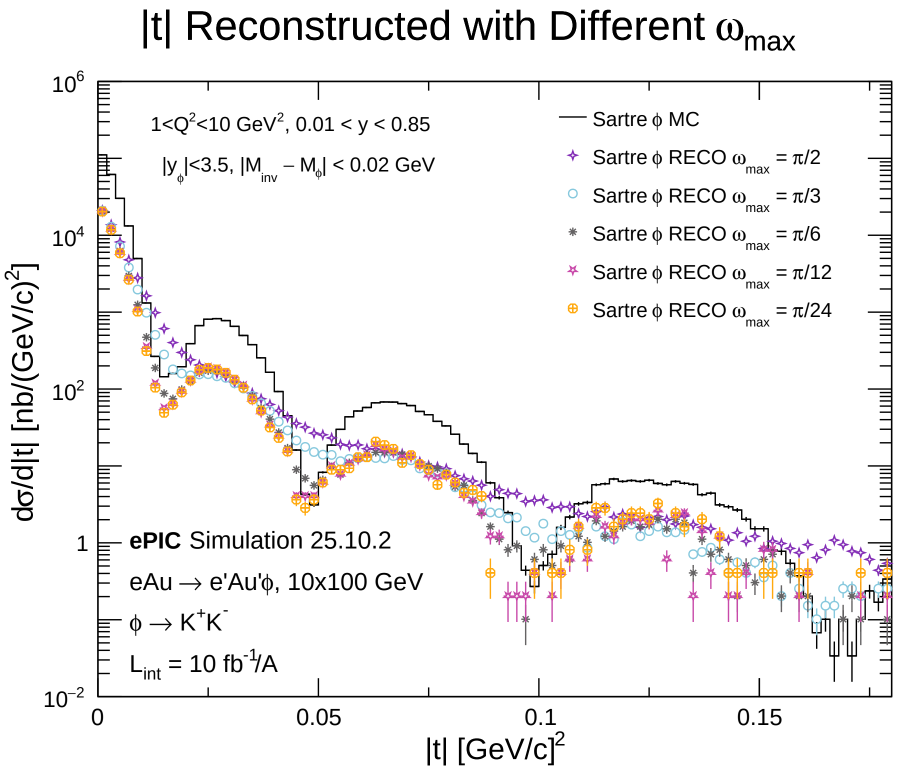

Figure 23: $|t|$ distribution for different $\omega_{\max}$ values. $\omega_{\max} = \pi/2$ is equivalent to method L. As we decrease the amount of phase space that we keep in our measurement, the diffractive pattern becomes more prominent. The solid black curve corresponds to the MC truth, purple open double diamonds for $\omega_{\max} = \pi/2$, open blue circles for $\omega_{\max} = \pi/3$, gray stars for $\omega_{\max} = \pi/6$, open pink stars for $\omega_{\max} = \pi/12$, and yellow octagons with a cross for $\omega_{\max} = \pi/24$.

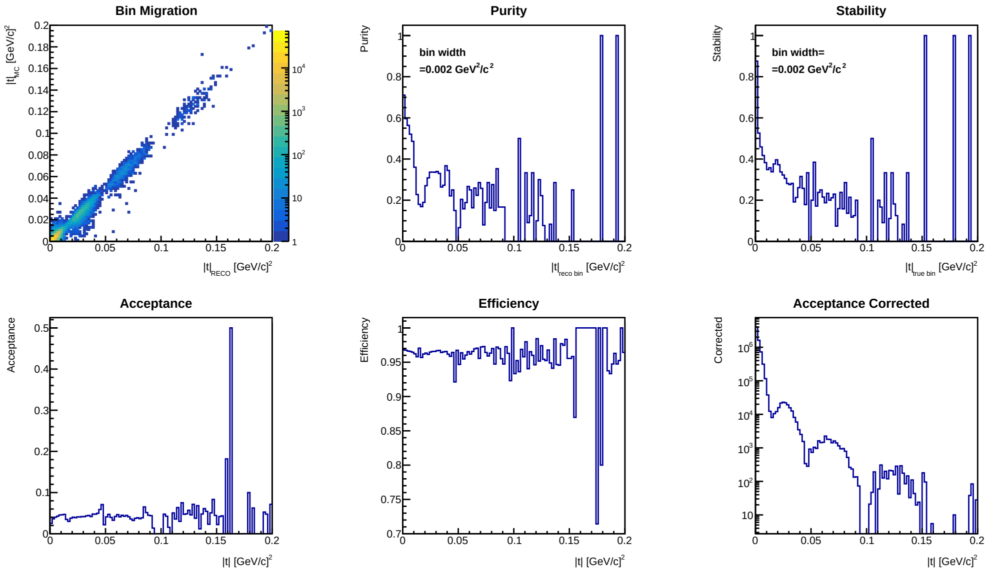

Figure 24: QA plots for the $|t|$ distribution reconstructed using the projection method derived from Eqs. 27 and 29. Here we have used a $\omega_{\max} = \pi/12$ wedge cut.

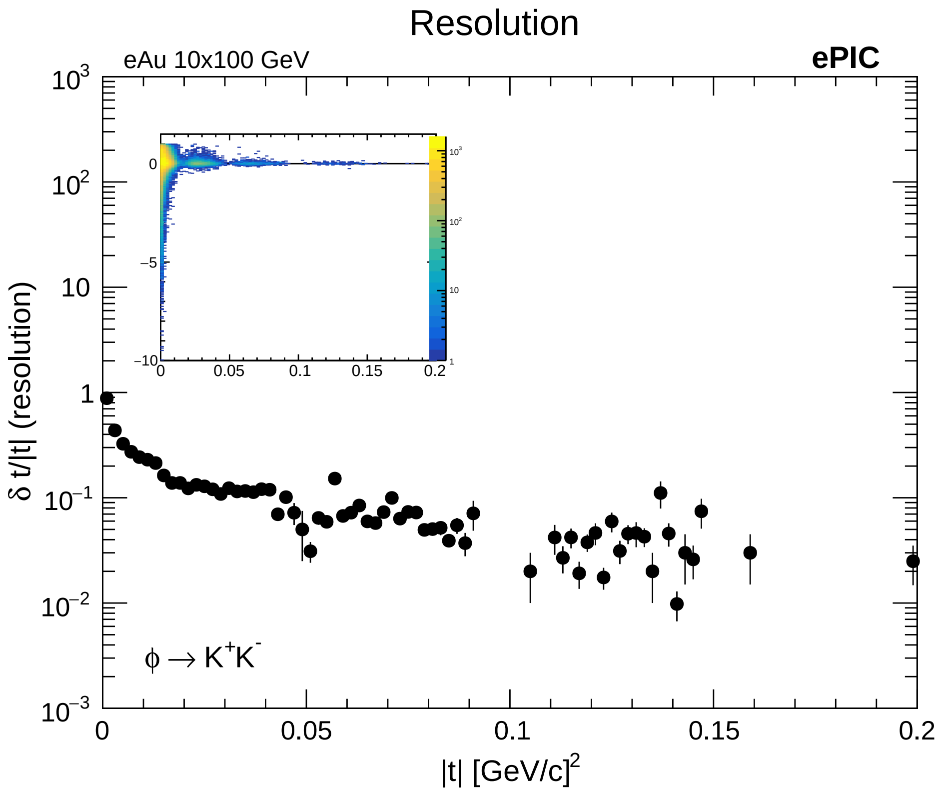

Figure 25: Resolution of the $|t|$ distribution. The inset shows the 2D resolution where the x-axis is $|t|_{\mathrm{MC}}$ and the y-axis is given by $(|t|_{\mathrm{MC}} - |t|_{\mathrm{proj}})/|t|_{\mathrm{MC}}$.

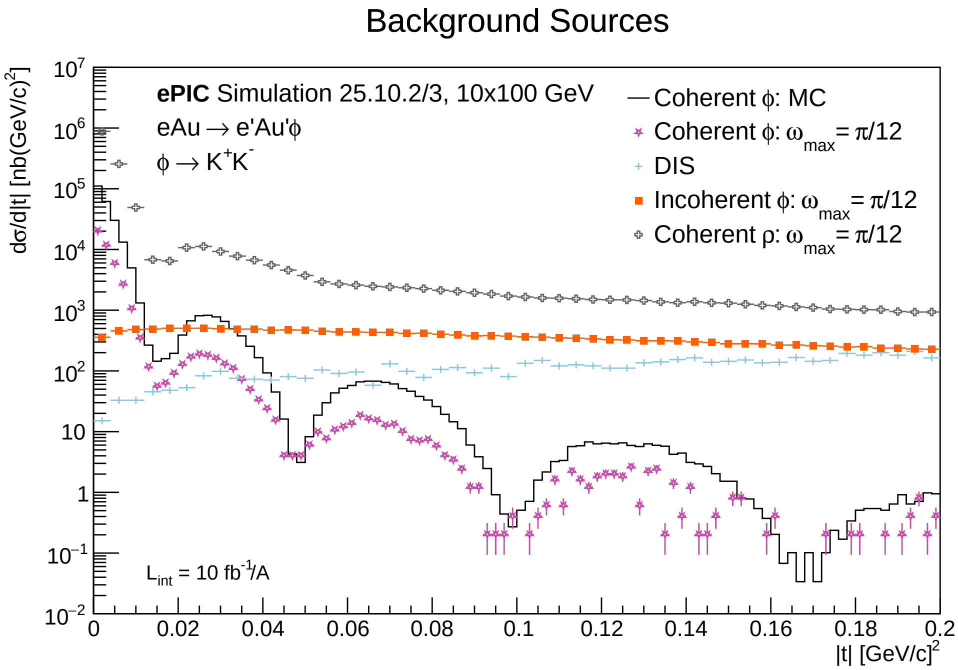

Figure 26: $|t|$ distribution with all systematic uncertainties studied in the analysis without any vetoes, cuts, or PID applied. The black solid curve represents the MC truth distribution, the open pink stars correspond to the projection method, light blue plus signs for the DIS distribution, solid orange squares for the incoherent ϕ production, and the open gray cross for the ρ production.

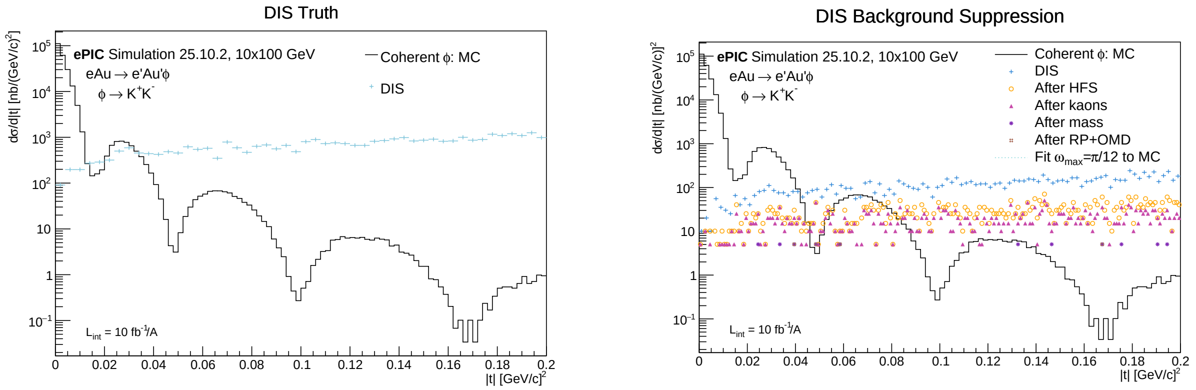

Figure 27: $|t|$ distribution with DIS background shown as the light blue plus signs and the MC truth is the black solid line. The rightmost plot shows the progression of suppression with each additional cut or veto. The open yellow circles show the DIS distribution after the requiring exclusivity (HFS is only two tracks). The red filled triangles show the distribution after requiring that those two tracks are kaons. The filled purple stars represent the distribution and the mass selection and open brown squares show the distribution after all detector vetoes are applied. Lastly, the cyan dashed line shows the fit distribution from the projection method with a wedge cut of $\omega_{max} = \pi/12$ after all vetoes and cuts are applied.

background is removed. Figure 27 shows the progression of DIS background removal from each detector veto and cut. For the detector vetoes, we use the OMD and RP detectors in this analysis. Note that at the time of this analysis, there are no ZDC for the DIS files. We also require that the HFS only contains the decay daughters. We see from Fig. 28 that the cuts and vetoes remove most of the DIS background. We have 38 events remaining in the projected $|t|$ distribution so we use a fit to the DIS truth distribution.

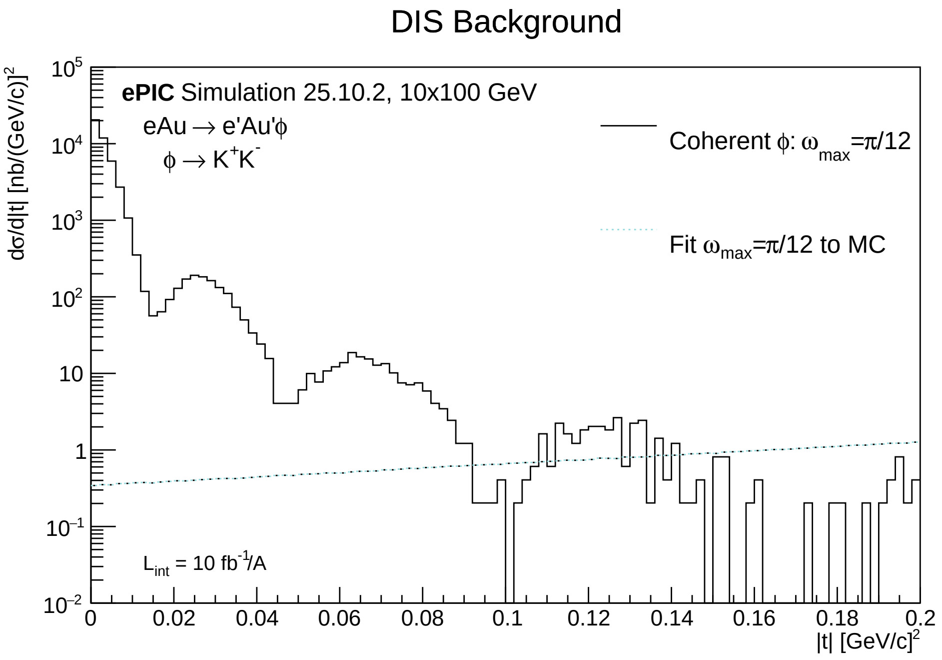

Figure 28: Coherent $|t|$ distribution reconstructed using the projection method with a wedge cut of $\omega_{max} = \pi/12$ shown as the black curve. The cyan dashed line shows the reconstructed distribution using the projection method with a wedge cut of $\omega_{max} = \pi/12$ after all vetoes and cuts have been applied.

3.3.2 ρ Production

Another source of systematic uncertainty is the production of the ρ VM. Figure 31 shows the $|t|$ distribution with the included ρ contamination. After implementing PID using the branch `ReconstructedChargedParticles.PDG`, we observe that the projection method is able to remove all of the ρ production.

Figure 29 shows the VM mass distributions with and without PID. We see that without PID, the selection on the ϕ mass successfully reduces the number of ρ particles but there still remains a significant amount of misidentified ρ particles. Figure 30 shows the $|t|$ distribution of the misidentified ϕ without using PID. Again, we can only resolve the first minima after implementing all selection cuts and vetoes. However, upon implementing PID, we are able to remove all of the ρ background as shown in Fig. 31.

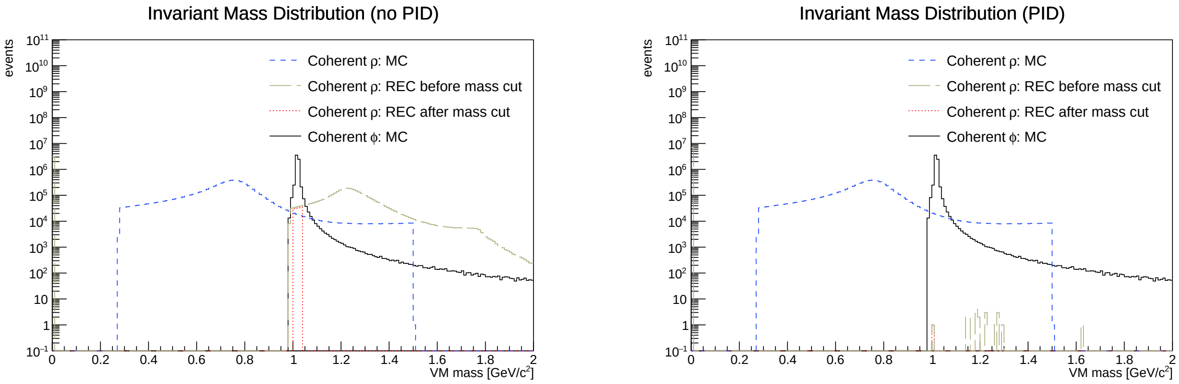

Figure 29: The leftmost plot shows the mass distributions of ρ and ϕ with no PID while the rightmost plot shows the same distributions with PID. The blue dashed curve is for the MC ρ distribution, the long dashed green curve shows the distribution of ρ reconstructed before any mass selection, the dashed orange curve shows the ρ distribution after the mass selection, and the solid black line shows the MC ϕ distribution.

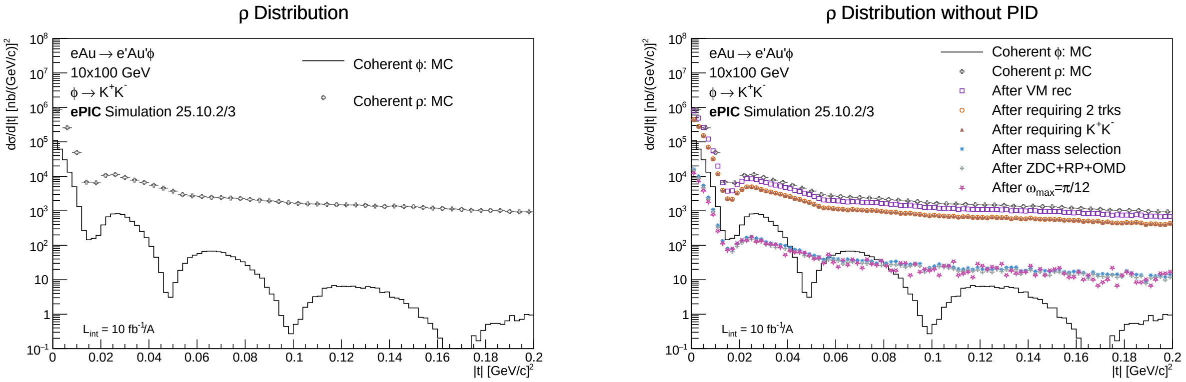

Figure 30: The leftmost plot shows the MC distributions for ϕ and ρ meson $|t|$ distributions. The black solid curve shows the ϕ distribution while the gray open plus signs show the ρ distribution. The rightmost plot shows the progression of ρ suppression with each cut and veto without using PID. The open purple squares show the $|t|$ distribution after reconstructing the VM. The open yellow circles show the distribution after requiring two tracks in the HFS, the brown filled triangles show the distribution after requiring that those two tracks are kaons. The filled blue stars show the distribution after the mass selection and the gray plus sign shows the distribution after applying all detector vetoes. Lastly, the open pink stars show the $|t|$ reconstructed distribution using the projection method with a wedge cut of $\omega_{max} = \pi/12$.

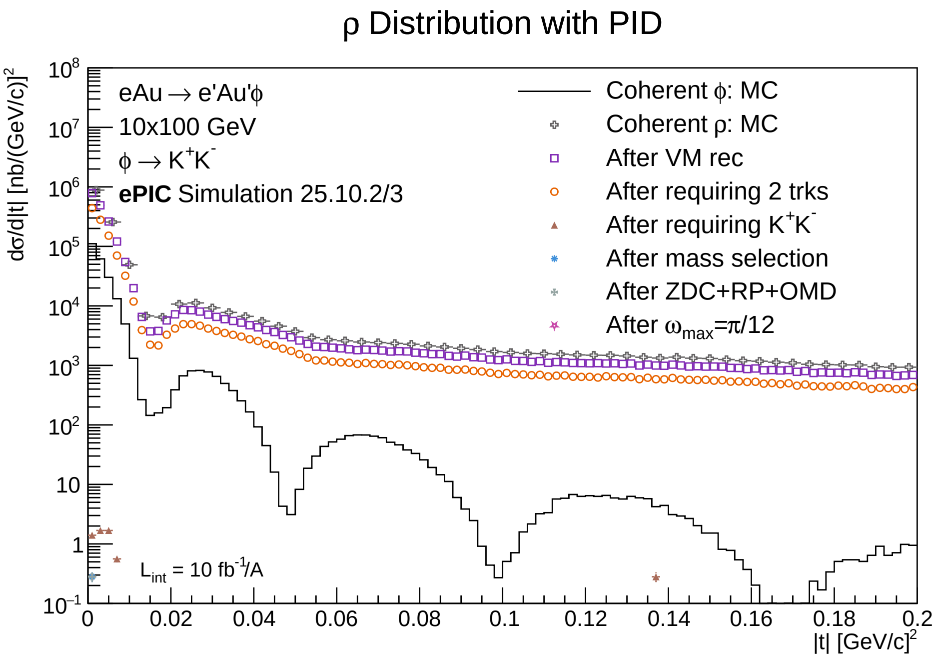

Figure 31: $|t|$ distribution with ρ production. The curves are represented in the same way as Fig. 30 except this plot shows the distributions using PID in the ϕ reconstruction.

3.3.3 Incoherent Production

The dominate source of systematic uncertainty in this analysis arises from the incoherent production. As shown in Fig. 32, we see that the incoherent background dominates our diffractive pattern in the $|t|$ distribution. After implementing the detector vetoes and cuts as mentioned in Section 3.3.1, with the additional of ZDC vetoes, we see some suppression, as shown in Fig. 32 but there is still an overwhelming amount of incoherent production remaining. The final distribution of coherent to incoherent is shown in Fig. 33. Following the proposed spin-based technique in [4], we plan to statistically remove this background in the future.

3.4 Analysis Code

- Code found on GitHub [16] where you will find:
  - The analysis code used for this note
  - Plot macros to reproduce all plots in this note
  - A script to get the same input filelists used in this note
- Detailed instructions for running the code locally or through condor are found in the README.

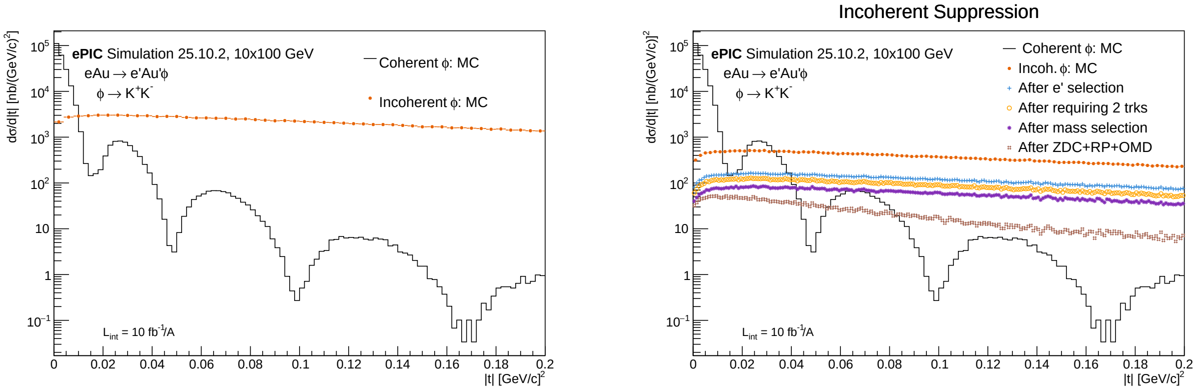

Figure 32: $|t|$ distribution with incoherent production. The black solid curve represents the coherent MC truth while the the filled orange squares are for the incoherent production distribution. The leftmost plot shows the distribution with no vetoes or cuts applied. The rightmost plot shows the suppression of incoherent production as each veto or cut is applied. The cyan plus symbol shows the $|t|$ distribution after we have reconstructed the scattered electron, the open yellow circles show the distribution after requiring only two tracks, the purple filled stars show the distribution after our mass selection, and the open brown squares show the distribution after all detector vetoes have been applied.

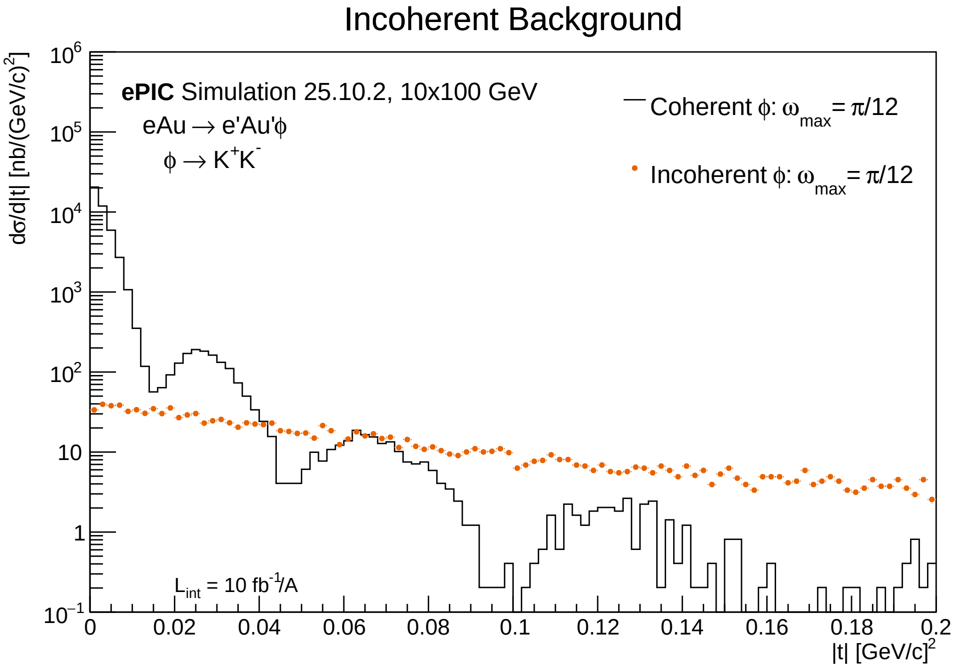

Figure 33: Coherent and incoherent $|t|$ distributions. The coherent curve, shown as the black line, has been reconstructed using the projection method with a wedge cut of $\omega_{max} = \pi/12$. The filled orange circles show the distribution after all vetoes and cut have been applied and $|t|$ has been reconstructed also using the projection method with a wedge cut of $\pi/12$.

4 Results and Discussion

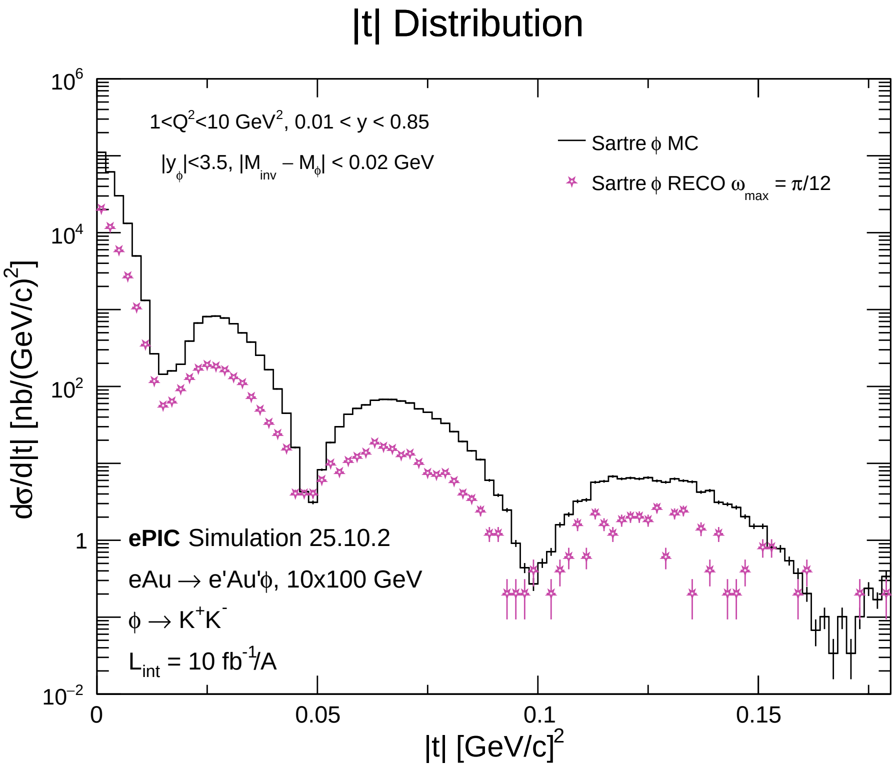

Figure 34: $|t|$ distribution after applying a cut of $\omega = \pi/12$. This plot shows the improvement of the $|t|$ measurement by comparing the coherent truth (MC reconstruction, black curve) with the new projection method (open pink stars).

The results of the $|t|$ distribution reconstruction are shown in Figs. 34 and 36. First, we can see a significant enhancement in resolving the diffractive pattern of the $|t|$ distribution. Previously, the best method available for us to use was method L as stated in [15]. The projection method enables us to determine the peaks and minima with a much better resolution than before. The price we pay for making the wedge cut in the projection method is a loss of statistics. In this example, we use $\omega_{max} = \pi/12$ which results in $\approx 83\%$ of lost coherent VM events. Second, Fig. 36 clearly indicates an improvement from the method L reconstruction. Figure 35 show the comparison of other $|t|$ reconstruction techniques with the MC and projection + wedge cut distributions. These transformations demonstrate the importance of resolving the diffractive minima precisely to result in a more accurate transformation.

This analysis demonstrates that the projection method used to reconstruct the momentum distribution is an effective approach to overcome the previous challenges of the $|t|$ measurement and allows more precise spatial imaging of the gluons inside the nucleus. In future work we will statistically separate the coherent and incoherent events to reduce the incoherent background. The outcome will be a complete analysis technique for the measurement of the $|t|$ distribution.

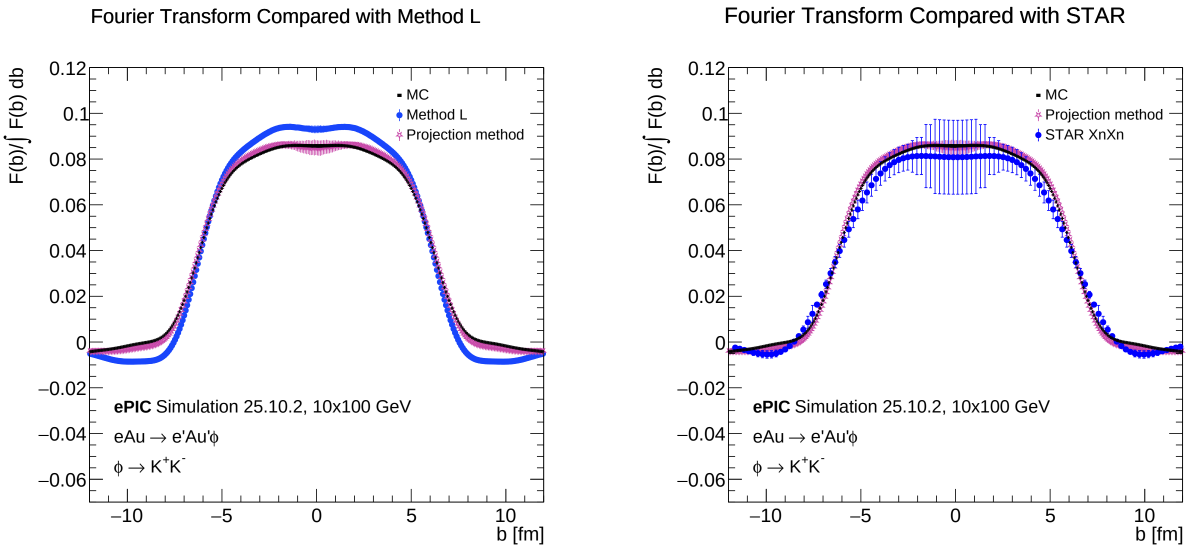

Figure 35: 2-dimensional Fourier-Bessel transformation of the $|t|$ distribution. This shows the gluon spatial distribution with a comparison from the transforms of the truth, method L, and the projection method distributions. The black solid curve represent the truth distribution and the pink open stars represent the reconstruction of $|t|$ using the new projection technique. The leftmost plot shows $|t|$ reconstruction using method L shown as the curve with filled blue circles. The rightmost plot shows the $XnXn$ curve from Fig. 9b in [1] as the blue filled circles as comparison.

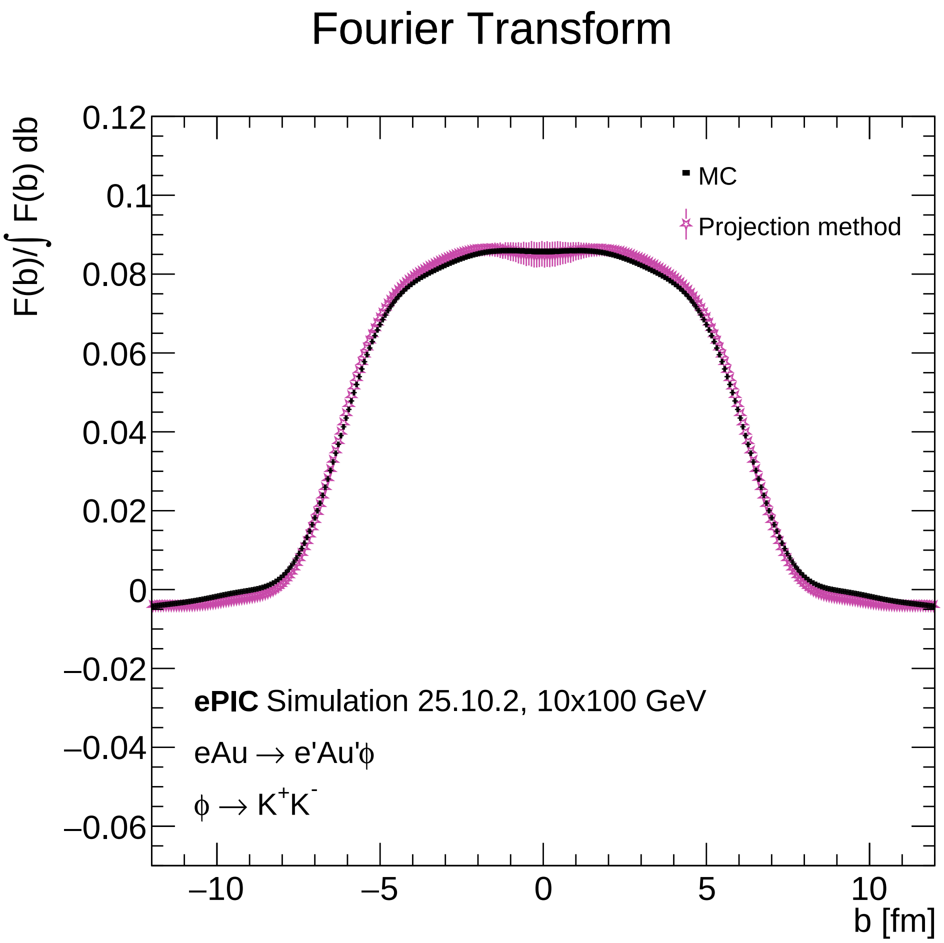

Figure 36: Gluon spatial distribution from the Fourier transformation of the MC $|t|$ distribution, shown as the black curve and from the projection method with a wedge cut of $\omega_{max} = \pi/12$ shown as the open pink stars.

References

[1] STAR, L. Adamczyk *et al.*, Phys. Rev. C **96**, 054904 (2017), 1702.07705.

[2] A. Accardi *et al.*, Eur. Phys. J. A **52**, 268 (2016), 1212.1701.

[3] N. Armesto and A. H. Rezaeian, Phys. Rev. D **90**, 054003 (2014), 1402.4831.

[4] M. Kesler *et al.*, (2025), 2502.15596.

[5] T. Toll and T. Ullrich, Phys. Rev. C **87**, 024913 (2013), 1211.3048.

[6] STAR Collaboration, L. Adamczyk *et al.*, Phys. Rev. C **96**, 054904 (2017).

[7] Reconstruction campaigns, Accessed: November 10, 2025.

[8] S. Rahman, Accessed: December 15, 2025.

[9] T. Toll and T. Ullrich, Comput. Phys. Commun. **185**, 1835 (2014), 1307.8059.

[10] T. Toll and T. Ullrich, Sartre: Event generator for diffractive processes in ep and ea collisions, 2018, Accessed: July 15, 2025.

[11] Sartredataset, Accessed: August 1, 2025.

[12] Z. Tu, Beaglesamples, 2025, Accessed: August 1, 2025.

[13] E. Aschenaue, M. Baker, J. H. Lee, and Z. Tu, Beagle, Accessed: July 10, 2025.

[14] W. Lin, Accessed: November 26, 2025.

[15] R. Abdul Khalek *et al.*, Nuclear Physics A **1026**, 122447 (2022).

[16] M. Kesler, epic-an-ac-2025-001, 2026, Accessed: March 16, 2026.